THE JOURNAL OF
PHYSICAL CHEMISTRY A

Article

pubs.acs.org/JPCA

Slow Photoelectron Velocity-Map Imaging Spectroscopy of the *ortho*-Hydroxyphenoxide Anion

Marissa L. Weichman,[†] Jongjin B. Kim,[†,§] and Daniel M. Neumark*[,†,‡]

[†]Department of Chemistry, University of California, Berkeley, California 94720, United States

[‡]Chemical Sciences Division, Lawrence Berkeley National Laboratory, Berkeley, California 94720, United States

S *Supporting Information*

ABSTRACT: We report high-resolution photodetachment spectra of cryogenically cooled *ortho*-hydroxyphenoxide anions (o-$HOC_6H_4O^-$) using slow photoelectron velocity-map imaging spectroscopy (cryo-SEVI). We observe transitions to the three lowest-lying electronic states of the *ortho*-hydroxyphenoxy radical, and resolve detailed vibrational features. Comparison to Franck–Condon simulations allows for clear assignment of vibronic structure. We find an electron affinity of 2.3292(4) eV for the neutral $\tilde{X}^2A''$ ground state, improving upon the accuracy of previous experiments. We measure term energies of 1.4574(7) eV and 1.5922(48) eV for the $\tilde{A}^2A'$ and $\tilde{B}^2A''$ excited states respectively, representing their first resolution and clear assignment. Photodetachment threshold effects are considered to explain the structure of these bands.

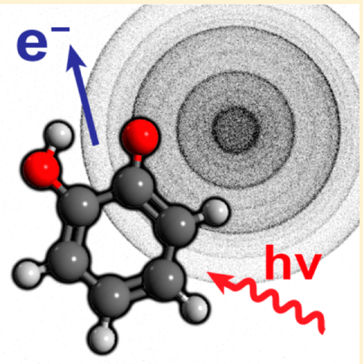

I. INTRODUCTION

Hydroxybenzenes are important ultraviolet (UV) chromophores in key biomolecules. In general, the presence of heteroatoms greatly complicates the electronic structure of aromatic species. Characterizing excited state surfaces and the dynamics of nonradiative relaxation pathways in these species can elucidate the chemistry subsequent to photoexcitation of biological systems.[1−3]

In this work, we focus on derivatives of catechol (1,2-dihydroxybenzene). Catechol moieties are present in antioxidants,[4−7] the hormones dopamine and adrenaline, and the pigment eumelanin,[8,9] which is thought to be involved in photoprotection of human skin through dissipation of energy after UV irradiation.[10] Catechols also have a proclivity to form complexes with metals in solution, as they can bind with a bidentate motif.[11] Here, we report a high-resolution photodetachment study of deprotonated catechol, the *ortho*-hydroxyphenoxide (o-HPO^-) anion, revealing detailed vibronic structure of the *ortho*-hydroxyphenoxy (o-HPO) radical.

The o-HPO radical (Figure 1) is of interest as a photodissociation product of catechol, the photochemistry of catechol being a useful model for that of larger biomolecules. In 2012, King et al.[12] used H atom Rydberg tagging photofragment translational spectroscopy to study photoexcitation of catechol, probing H-loss and formation of ground state o-HPO radicals. The final vibrational states of o-HPO were highly dependent on torsional excitation of the free OH moiety in the $^1\pi\pi^*$ (S_1) state of catechol prior to dissociation along the $^1\pi\sigma^*$ (S_2) surface. While internal energies of the o-HPO products were measured, no definitive assignment of vibrational modes was made. Soon afterward, Chatterley et al.[13] published an ultrafast time-resolved ion imaging study of the photodissociation of catechol. The authors observed the formation of ground state o-HPO radicals via tunneling from the S_1 state of catechol to the dissociative S_2 state at energies below the S_1/S_2 conical intersection. Livingstone et al.[14] and Weiler et al.[15] also reported short lifetimes of photoexcited catechol, and ascribed them to dissociation to o-HPO + H mediated by this tunneling process.

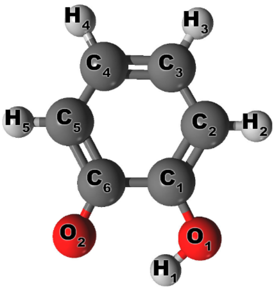

Figure 1. Structure of *ortho*-hydroxyphenoxy.

The o-HPO radical itself has been studied experimentally with electron spin resonance spectroscopy,[16,17] and IR spectroscopy in an argon matrix, wherein many IR active vibrational modes were identified.[18] Several studies have reported calculated geometries, energetics, vibrational frequencies, and reactivity of o-HPO.[19−25] The o-HPO^- anion is less

Special Issue: Jean-Michel Mestdagh Festschrift

Received: January 24, 2015
Revised: March 5, 2015
Published: March 6, 2015

DOI: 10.1021/acs.jpca.5b00768
J. Phys. Chem. A 2015, 119, 6140−6147

well-characterized than its radical counterpart. One theoretical study found a calculated barrier of approximately 2360 cm^{-1} for intramolecular transfer of the proton between the two O atoms in *o*-HPO^-,[26] sufficiently large to make proton tunneling negligible. Experimental work has studied collision-induced fragmentation of *o*-HPO^-[27] and the kinetics of its reactions with BF_3 and SiF_4.[28] A study by Fattahi et al.[29] estimated the electron binding energy and proton affinity of *o*-HPO^- through bracketing with numerous ion−molecule reactions.

Photoelectron spectroscopy (PES) is an attractive technique for gaining spectroscopic access to reactive radicals through photodetachment of a closed-shell anion.[30] The PES spectrum of *o*-HPO^- was measured by Wang et al.[25] in 2010, who found an electron affinity (EA) of 2.315(10) eV for the radical ground state, and Franck−Condon (FC) vibrational activity in modes with frequencies of 605(40) cm^{-1} and 1575(40) cm^{-1}. The authors also observed several radical electronic excited states, but could not make definitive assignments.

We report high-resolution slow photoelectron velocity-map imaging (SEVI) spectra of detachment to the ground and two lowest excited electronic states of *o*-HPO, as part of an ongoing effort to characterize complex aromatic radicals.[31,32] More specifically, the present study can be considered an extension of our work on the phenoxy system,[33] with an added hydroxyl group in the ortho position and correspondingly more complex electronic structure. *o*-HPO^- anions are buffer-gas cooled in an ion trap at 5 K prior to photodetachment which, in combination with the characteristic SEVI energy resolution of <4 cm^{-1}, reveals detailed vibrational and electronic information. We obtain an accurate EA of the neutral $\tilde{X}$ state, term energies of the $\tilde{A}$ and $\tilde{B}$ electronic bands, and several fundamental vibrational frequencies.

II. EXPERIMENTAL METHODS

The cryo-SEVI method has been described in detail previously.[34−36] Briefly, we photodetach cryogenically cooled and mass-selected anions with tunable light and measure the kinetic energy distribution of the resulting photoelectrons with a velocity-map imaging (VMI) spectrometer. At low VMI extraction voltages, slow electrons are preferentially detected, and their image is magnified on the detector, resulting in sub-millielectronvolt energy resolution.

o-HPO^- anions are prepared by expanding a dilute gas mixture of catechol through a pulsed Even−Lavie solenoid valve[37] fitted with a circular filament ionizer. The catechol precursor is stored in a cartridge heated to 90 °C. A gas mixture of trace NF_3 in 150 psi of He flows through the cartridge and carries the catechol vapor through the valve into the vacuum chamber. Electrons from the ionizer induce dissociative attachment of NF_3 to form F^-, which deprotonates catechol to form the desired *o*-HPO^- anions. The anions are directed through an RF hexapole ion guide and a quadrupole mass filter, and into a linear octopole ion trap. The trap is held at 5 K, and filled with pulsed bursts of precooled He/H_2 buffer gas in an 80:20 mixture. The ions are stored for 40 ms, enabling collisional cooling to their ground vibrational state. Under these conditions, we have measured molecular ion temperatures as low as 10 K at the time of photodetachment.[36] The ions are extracted from the trap into an orthogonal Wiley−McLaren time-of-flight mass spectrometer.[38] The mass-selected ion packet is then photodetached with the output of an Nd:YAG-pumped tunable dye laser operating at a repetition rate of 20 Hz. Resulting photoelectrons are focused with a low-voltage VMI electrostatic lens[39] onto a detector comprising two chevron-stacked microchannel plates (MCPs) coupled to a phosphor screen;[40] events on the screen are recorded with a CCD camera.

We use event counting software to identify single electron events and compute their centroids after each laser shot during data acquisition.[41] The radial and angular electron distributions are reconstructed from the accumulated image using the Maximum Entropy Velocity Legendre Reconstruction (MEVELER) method.[42] The distance of an electron spot from the center of the reconstructed image is linearly proportional to its velocity after photodetachment. The spectrometer is calibrated with SEVI images of well-characterized photodetachment transitions of atomic S^- and Cl^-,[43−45] in order to relate radial position in the image to electron kinetic energy (eKE). As the eKE is a function of photodetachment laser energy ($h\nu$), we report SEVI spectra in electron binding energy (eBE), given by eBE = $h\nu$ − eKE.

The VMI spectrometer has a roughly constant resolving power ΔeKE/eKE, thereby yielding the best resolution for low-eKE transitions. As described previously,[31] we first measure a low-resolution overview spectrum at a single photon energy well above the band of interest. We then obtain high-resolution spectra over narrow eKE windows by recording images at discrete photodetachment energies tuned 20−40 cm^{-1} above spectral features of interest, using lower VMI voltages to magnify these images as much as possible. These windows are spliced together to create a composite high-resolution spectrum of the region spanned by the overview spectrum. The high-resolution trace of a given feature is scaled to the intensity of that feature in the overview spectrum so as to avoid any threshold effects that may distort peak intensities.

III. CALCULATIONS

Electronic structure calculations for the ground state of the *o*-HPO^- anion and the three lowest-lying states of the *o*-HPO radical were carried out with density functional theory (DFT), in order to find the energetics, optimized geometries, normal modes, and harmonic vibrational frequencies of all relevant states. The B3LYP functional was used in combination with the Pople-style 6-311+G* basis set, as this level of theory has proved effective for other aromatic systems studied in our lab.[31,32] The maximum overlap method (MOM)[46] was used for the first two excited states of the radical. In order to avoid root-flipping issues for MOM excited state calculations, an integration grid with 128 radial quadrature points and 302 angular quadrature points was used for the exchange-correlation integrand. Dyson orbitals for photodetachment transitions were calculated with EOM-IP-CCSD/6-311+G*. All ab initio calculations were carried out in Q-Chem 4.0.[47,48]

The *o*-HPO^- anion is a closed-shell species, with an electronic molecular orbital (MO) configuration described by $...(4a'')^2(24a')^2(5a'')^2$. Both MOM and EOM-IP-CCSD calculations indicate that detachment from the anion $5a''$ MO yields the $\tilde{X}^2A''$ radical ground state, detachment from the $24a'$ MO yields the $\tilde{A}^2A'$ state, and detachment from the $4a''$ MO gives the $\tilde{B}^2A''$ state. Dyson orbitals for these three detachment transitions are shown in Figure 2. The $5a''$ and $24a'$ orbitals have *p*-like lobes on the oxygen radical site that are out-of-plane and in-plane, respectively; they are analogous to the singly occupied MOs in the $\tilde{X}^2B_1$ and $\tilde{A}^2B_2$ states of the phenoxy radical.[33,49,50]

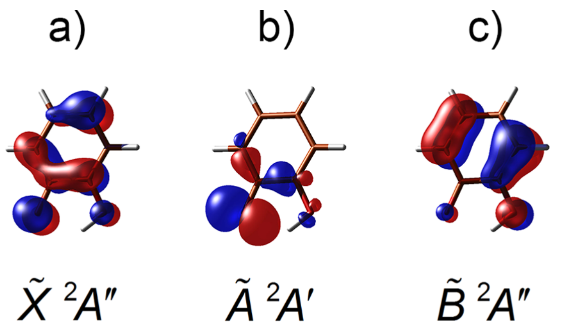

Figure 2. Dyson orbitals for detachment from the $\tilde{X}\,^1A'$ *ortho*-hydroxyphenoxide anion to the (a) $\tilde{X}\,^2A''$, (b) $\tilde{A}\,^2A'$, and (c) $\tilde{B}\,^2A''$ neutral states.

Calculated energetics corrected for vibrational zero-point energy and relevant harmonic vibrational frequencies are summarized in Table 1, while full lists of optimized geometries and calculated harmonic frequencies can be found in Tables S1 and S2 of the Supporting Information. Geometries of all states were restricted to internally H-bonded, planar C_s structures (see Figure 1), as recommended by the literature.[19−22,24,25] The anion ground state and the neutral $\tilde{X}$ and $\tilde{A}$ states were found to have planar equilibrium geometries. The optimized neutral $\tilde{B}$ state planar structure was found to have a small imaginary out-of-plane frequency (labeled ν_{33} in Table S2). A one-dimensional slice of the $\tilde{B}$ state potential along the ν_{33} normal mode coordinate was calculated with time-dependent DFT (TDDFT).[51] The ν_{33} potential is a shallow double well, with the planar geometry resting on top of a 74 cm^{-1} barrier. The one-dimensional ν_{33} potential was fit to an eighth order polynomial, and energy eigenvalues were solved for numerically. The ν_{33} vibrational zero-point energy was found to lie 63 cm^{-1} above the planar geometry barrier. We therefore treat the radical $\tilde{B}$ state as an effectively planar species.

Table 1. B3LYP/6-311+G* Calculated Energetics and Relevant Harmonic Vibrational Frequencies for the *ortho*-Hydroxyphenoxy Radical

state	parameter	calculated
$\tilde{X}\,^2A''$	EA,[a] eV	2.2317
	ω_8, cm^{-1}	1529
	ω_9, cm^{-1}	1493
	ω_{12}, cm^{-1}	1337
	ω_{13}, cm^{-1}	1265
	ω_{20}, cm^{-1}	579
	ω_{21}, cm^{-1}	566
	ω_{22}, cm^{-1}	450
	ω_{23}, cm^{-1}	331
$\tilde{A}\,^2A'$	TE,[b] eV	1.4512
	ω_{12}, cm^{-1}	1254
	ω_{13}, cm^{-1}	1214
	ω_{21}, cm^{-1}	523
	ω_{23}, cm^{-1}	289
	ω_{24}, cm^{-1}	927
$\tilde{B}\,^2A''$	TE, eV	1.5631

[a] Electron affinity. [b] Term energy.

Photoelectron spectra for detachment to all three neutral states were simulated using the ezSpectrum program.[52] The DFT geometries, normal modes, and harmonic frequencies were given as input, and FC overlap factors were calculated in the harmonic approximation with Duschinsky mixing[53] of all modes. The vibrational origins of the three simulated electronic bands were shifted to the experimentally assigned values, and simulated intensities were scaled to match the first peak in each experimental band. Those frequencies of the neutral $\tilde{X}$ and $\tilde{A}$ states that were observed in the high-resolution SEVI spectra were scaled to their experimental values; the others were left at their calculated B3LYP/6-311+G* values. In the radical $\tilde{B}$ state, the ν_{33} mode, along which the potential is a shallow double well, is not FC active, and its anharmonicity therefore has no significant impact on the simulation.

The photoelectron angular distribution (PAD) of the photodetachment transition to the $\tilde{X}$ state and cross sections for detachment to the $\tilde{A}$ and $\tilde{B}$ states were calculated as functions of eKE with the ezDyson program,[54,55] which uses ab initio calculated Dyson orbitals to find the contribution of partial spherical waves with angular momentum $l \leq 4$ to the wave function of the outgoing photoelectron.

IV. RESULTS

Overview SEVI spectra of the *o*-HPO$^-$ anion photodetachment are shown in blue in Figure 3 for two regions of binding energy. Accompanying FC simulations, broadened appropriately to match the experimental resolution, are given in gray. High-resolution spectra of photodetachment to the lower energy band are presented in Figure 4, while higher binding energy spectra are shown in Figure 5. In Figures 4 and 5, the higher-resolution traces shown in black are scaled to the intensity profile of the overview and vertically offset. FC stick simulations are shown in red and green. All spectra presented here were taken with an ion trap temperature of 5 K.

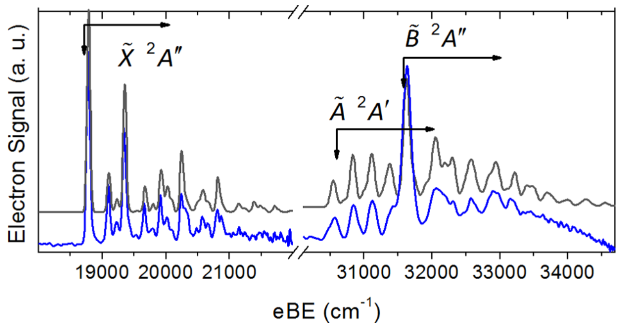

Figure 3. Low-resolution SEVI spectra of transitions to the $\tilde{X}$, $\tilde{A}$, and $\tilde{B}$ states of the *ortho*-hydroxyphenoxy radical (blue). The overview of the ground state was taken at a photon energy of 22236 cm^{-1}, while the excited state overview is the average of two traces taken at 34720 and 34750 cm^{-1}. FC simulations (gray) are broadened by a Gaussian distribution with fwhm 60 cm^{-1} for the $\tilde{X}$ state, and fwhm 100 cm^{-1} for the $\tilde{A}$ and $\tilde{B}$ states.

The photodetachment band in Figure 4 has an intense onset of structure at peak A, with weaker vibrational structure continuing for about 4000 cm^{-1}. Positions and assignments for the peaks labeled in Figure 4 are summarized in Table 2, and discussed in detail in Section V. Peak positions represent the center of a Gaussian fit. The narrowest features in this band have a full width at half-maximum (fwhm) of 7−8 cm^{-1}; this is typical of the resolution of SEVI for molecular systems.[31,56]

Figure 5 shows higher-resolution spectra of the features at higher binding energy. The appearance of the intense peak *x* in

DOI: 10.1021/acs.jpca.5b00768
J. Phys. Chem. A 2015, 119, 6140−6147

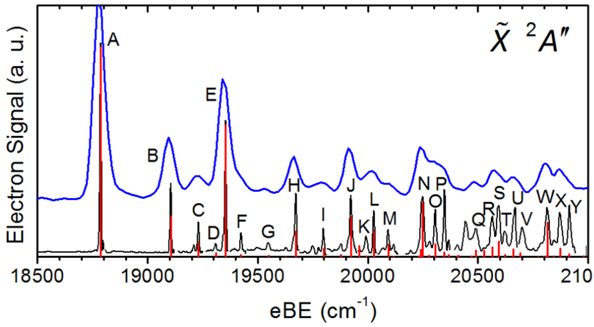

Figure 4. SEVI spectra of the $\tilde{X}^2A'' \leftarrow \tilde{X}^1A'$ photodetachment of *ortho*-hydroxyphenoxide. The blue trace is the low-resolution overview spectrum from Figure 3; the black traces are high-resolution spectra taken at many laser frequencies. An FC simulation stick spectrum is shown in red.

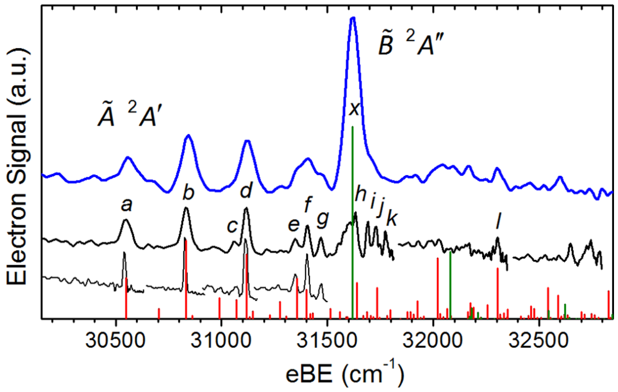

Figure 5. SEVI spectra of the $\tilde{A}^2A' \leftarrow \tilde{X}^1A'$ and $\tilde{B}^2A'' \leftarrow \tilde{X}^1A'$ photodetachment transitions of *ortho*-hydroxyphenoxide. A low-resolution spectrum is shown in blue, while black traces are medium- and high-resolution spectra taken at many laser frequencies. FC simulation stick spectra are shown in red for the $\tilde{A}^2A' \leftarrow \tilde{X}^1A'$ band, and in green for the $\tilde{B}^2A'' \leftarrow \tilde{X}^1A'$ band.

Table 2. Peak Positions, Shifts, and Assignments for the SEVI Spectra of the $\tilde{\mathbf{X}}^2A'' \leftarrow \tilde{\mathbf{X}}^1A'$ Photodetachment of *ortho*-Hydroxyphenoxide Given in Figure 4

peak	position (cm^{-1})	shift (cm^{-1})	assignment
A	18787	0	0_0^0
B	19105	318	23_0^1
C	19230	444	22_0^1
D	19309	523	21_0^1?
E	19354	568	20_0^1
F	19424	638	23_0^2
G	19547	761	$22_0^1 23_0^1$
H	19673	886	$20_0^1 23_0^1$
I	19799	1012	$20_0^1 22_0^1$
J	19923	1136	20_0^2
K	19992	1205	$20_0^1 23_0^2$
L	20026	1240	13_0^1
M	20091	1305	12_0^1
N	20247	1461	9_0^1
O	20305	1519	8_0^1
P	20348	1561	$13_0^1 23_0^1$
Q	20488	1701	20_0^3
R	20564	1777	$9_0^1 23_0^1$
S	20592	1805	$13_0^1 20_0^1$
T	20622	1835	$8_0^1 23_0^1$
U	20664	1877	$12_0^1 20_0^1$
V	20692	1905	$9_0^1 22_0^1$
W	20814	2028	$9_0^1 20_0^1$
X	20873	2087	$8_0^1 20_0^1$
Y	20915	2128	$13_0^1 20_0^1 23_0^1$

Table 3. Peak Positions, Shifts, and Assignments for the SEVI Spectra of the $\tilde{\mathbf{A}}^2A' \leftarrow \tilde{\mathbf{X}}^1A'$ and $\tilde{\mathbf{B}}^2A'' \leftarrow \tilde{\mathbf{X}}^1A'$ Photodetachment Transitions of *ortho*-Hydroxyphenoxide Given in Figure 5

band	peak	position (cm^{-1})	shift (cm^{-1})	assignment
$\tilde{A}^2A' \leftarrow \tilde{X}^1A'$	*a*	30542	0	0_0^0
	b	30827	285	23_0^1
	c	31064	523	21_0^1
	d	31114	573	23_0^2
	e	31347	806	$21_0^1 23_0^1$
	f	31404	862	23_0^3
	g	31470	928	24_0^1?
	h	31633	1091	$21_0^2 23_0^1$
	i	31690	1148	23_0^4
	j	31728	1187	13_0^1?
	k	31775	1234	12_0^1?
	l	32304	1762	$13_0^1 23_0^2$?
$\tilde{B}^2A'' \leftarrow \tilde{X}^1A'$	*x*	31629	0	0_0^0

the midst of a weaker progression beginning with peak *a* suggests two overlapping electronic states. Positions and assignments (see Section V) for the peaks labeled in Figure 5 are summarized in Table 3. The best-resolved features in the progression beginning with peak *a* have a fwhm of ~13 cm^{-1} with the laser energy ~100 cm^{-1} above threshold. By contrast, peak *x* is fit best with a fwhm of 90 cm^{-1} with the laser energy set ~1800 cm^{-1} above, as its intensity dies away closer to threshold.

SEVI also yields anisotropies of photodetachment transitions. For a one-photon photodetachment process with linearly polarized light, the PAD is given by[57]

$$\frac{d\sigma}{d\Omega} = \frac{\sigma_{\text{tot}}}{4\pi}[1 + \beta P_2(\cos\theta)] \tag{1}$$

where θ is the angle relative to the polarization axis of the laser, P_2 is the second-order Legendre polynomial, and β is the anisotropy parameter, which varies between −1 for a PAD aligned perpendicular to the laser polarization and +2 for a PAD parallel to the laser polarization.

The PADs for all peaks in the *o*-HPO $\tilde{X}$ band have negative anisotropy parameters ($-0.5 < \beta < -0.1$) and become more isotropic close to threshold. Representative β values are plotted in Figure S1 as a function of eKE alongside ezDyson simulations. The PADs for the higher energy bands cannot be reported, as high-eKE photoelectrons from detachment to the $\tilde{X}$ state produce an overlapping signal that prevents reproduction of excited state anisotropies during image reconstruction.

V. DISCUSSION

The high-resolution *o*-HPO$^-$ spectra presented in Figures 4 and 5 are a clear demonstration of the efficacy of cryo-SEVI. The spectral resolution and clarity afforded by this technique allow us to untangle the combination of overlapping electronic states and dense FC structure seen here. We now discuss the assignments of the *o*-HPO$^-$ SEVI spectra, with comparison to simulation and the literature. All spectroscopic information obtained here is summarized and compared to prior work in Table 4.

Table 4. Experimental Parameters for the *ortho*-Hydroxyphenoxy Radical from the Current Work, with Comparison to Prior Experimental Literature Values

state	parameter	this work	prior work
$\tilde{X}^2A''$	EA,[a] eV	2.3292(4)[b]	2.315(10)[c]
	ν_8, cm^{-1}	1519(5)	1518[d]
	ν_9, cm^{-1}	1461(7)	1457[d]
	ν_{12}, cm^{-1}	1305(4)	1304[d]
	ν_{13}, cm^{-1}	1240(4)	1240[d]
	ν_{20}, cm^{-1}	568(3)	605(40)[c]
	ν_{21}, cm^{-1}	523(4)	
	ν_{22}, cm^{-1}	444(3)	
	ν_{23}, cm^{-1}	318(3)	
$\tilde{A}^2A'$	TE,[e] eV	1.4574(7)	
	ν_{12}, cm^{-1}	1234(6)	
	ν_{13}, cm^{-1}	1187(7)	
	ν_{21}, cm^{-1}	523(29)	
	ν_{23}, cm^{-1}	285(5)	
	ν_{24}, cm^{-1}	928(5)	
$\tilde{B}^2A''$	TE, eV	1.5922(48)	1.605(10)

[a] Electron affinity. [b] Uncertainties represent one standard deviation of a Gaussian fit to the experimentally observed peak. [c] Photoelectron spectroscopy, ref 25. [d] Matrix IR spectroscopy, ref 18. [e] Term energy.

The overview spectra of *o*-HPO$^-$ in Figure 3 exhibit two bands of vibronic structure separated by about 10,000 cm^{-1}. The lower energy band has a strong onset at low binding energy, while the structure of the higher energy band is not a simple FC envelope. An extended vibrational progression interrupted by one strong feature suggests photodetachment to two overlaid electronic states in the higher energy band. Cryogenic cooling prior to photodetachment ensures that we detach from the ground vibrational and electronic state of the *o*-HPO$^-$ anion. Hence, based on comparison with the electronic structure calculations discussed in Section III, we assign the lower band to the $\tilde{X}^2A'' \leftarrow \tilde{X}^1A'$ photodetachment, and the upper band to the overlapping $\tilde{A}^2A' \leftarrow \tilde{X}^1A'$ and $\tilde{B}^2A'' \leftarrow \tilde{X}^1A'$ transitions.

In Figure 4, peak A is assigned as the vibrational origin of the $\tilde{X}^2A'' \leftarrow \tilde{X}^1A'$ band. This yields an experimental EA of 2.3292(4) eV for the *o*-HPO radical, in good agreement with the B3LYP calculated EA of 2.2317 eV, and just outside the error bars of the experimental EA of 2.315(10) eV reported by Wang et al.[25] The FC envelope of the $\tilde{X}$ band also supports its assignment to detachment to the $\tilde{X}^2A''$ neutral state. The intense vibrational origin and weaker vibrationally excited FC structure suggests a small change in geometry upon photodetachment. Accordingly, there is only a slight displacement between the ground state anion and neutral optimized geometries reported in Table S1, and the Dyson orbital for this detachment (Figure 2a) is highly delocalized. Our recent report on the α- and β-naphthyl radicals also demonstrated that detachment from a delocalized π-system yields little FC activity, while detachment from an orbital localized predominantly on one atomic center yields significant disruption in geometry and an extensive FC envelope.[32]

Several fundamental frequencies of the radical ground state are observed (Table 4). Both the Gaussian-broadened FC simulation (Figure 3) and the FC stick spectrum (Figure 4) are in good agreement with the experimentally observed features, although the intensities of some overtones and combination bands are underrepresented, perhaps due to anharmonic effects. We report eight in-plane vibrational fundamentals: ν_{23} (peak B) with a frequency of 318 cm^{-1}, ν_{22} (peak C) at 444 cm^{-1}, tentatively ν_{21} (peak D) at 523 cm^{-1}, ν_{20} (peak E) at 568 cm^{-1}, ν_{13} (peak L) at 1240 cm^{-1}, ν_{12} (peak M) at 1305 cm^{-1}, ν_9 (peak N) at 1461 cm^{-1}, and ν_8 (peak O) at 1519 cm^{-1}. Schematics of normal mode displacements for these FC active vibrations are given in Figure S2a. This is the first report of the fundamental frequencies of modes ν_{21}, ν_{22}, and ν_{23}. While modes ν_8, ν_9, ν_{12}, ν_{13}, and ν_{20} have been previously identified with matrix IR spectroscopy[18] and/or PES[25] (see Table 4), this work represents their identification in a higher-resolution gas phase experiment.

The $\tilde{X}$ band is also observed to have a PAD polarized perpendicularly to the laser polarization axis ($\beta < 0$). For the detachment of large, low-symmetry molecules like *o*-HPO$^-$, the PAD cannot be easily predicted with group theory, so we turn to ab initio calculation and numerical simulation. The anisotropy parameter for the $\tilde{X}$ state was simulated as a function of eKE using the ezDyson program as described in Section III; the results are shown in Figure S1 and compared with the experimental anisotropy of the $\tilde{X}$ vibrational origin. Simulations reproduce PADs with negative β values over this range of eKE, although anisotropy calculations are very sensitive to the shape of the ab initio Dyson orbitals,[55] so the match in the value of β is only qualitative.

Figure 5 shows the high-resolution SEVI spectra of the higher binding energy photodetachment structure. Peak *a* is assigned to the vibrational origin of the $\tilde{A}^2A' \leftarrow \tilde{X}^1A'$ band. The experimental term energy of the $\tilde{A}$ state is therefore 1.4574(7) eV, in good agreement with the MOM-calculated value of 1.4512 eV. The *o*-HPO radical $\tilde{X}$ and $\tilde{A}$ states are more widely spaced than the analogous electronic states in phenoxy, which lie 0.952 eV apart.[50] Favorable interactions between the two O atoms in *o*-HPO stabilize the radical $\tilde{X}$ state with respect to the $\tilde{A}$ state, as evidenced by the nodal structure of the MOs in Figure 2a,b. The *o*-HPO $\tilde{A}$ state term energy is therefore raised with respect to that of phenoxy. Peak *x* in Figure 5 is assigned to the vibrational origin of the $\tilde{B}^2A'' \leftarrow \tilde{X}^1A'$ band, yielding an experimental $\tilde{B}$ state term energy of 1.5922(48) eV. This value is matched by an MOM calculated term energy of 1.5631 eV, and also lines up with the excited state reported by Wang et al.[25] at a term energy of 1.605(10) eV.

The $\tilde{A}$ band is dominated by a progression in the ν_{23} $O_1-C_1-C_6-O_2$ bending mode (peaks *b*, *d*, *f*, and *i*). This extended FC envelope indicates a significant change in geometry between the anion and the neutral $\tilde{A}$ states, as is reflected in the B3LYP optimized geometries (Table S1). The anion and $\tilde{A}$ state geometries differ particularly in the C_6-O_2 bond length and the $C_1-O_1-H_1$, $C_5-C_6-O_2$, and $C_5-C_6-C_1$ bond angles, consistent with localization of the $\tilde{A}$ state Dyson orbital to the C_6-O_2 bond and neighboring atoms (Figure 2b).

Assignments of all $\tilde{A}$ state vibrational features are detailed in Table 3. Schematics of FC active normal modes are given in Figure S2b, and their displacements involve distortions consistent with the change in geometry upon photodetachment. We observe the vibrational fundamentals ν_{23} (peak *b*) at 285 cm^{-1}, ν_{21} (peak *c*) at 523 cm^{-1}, and more tentatively ν_{13} (peak *j*) at 1187 cm^{-1} and ν_{12} (peak *k*) at 1234 cm^{-1}. There is no clear analogue in the simulation for peak *g*, which lies at 928 cm^{-1} above the $\tilde{A}$ origin; however, it lines up closely with the calculated frequency of the FC forbidden a'' symmetry ν_{24} mode. This mode could gain intensity through Herzberg–Teller (HT) coupling with totally symmetric vibrational levels of the nearby $\tilde{B}^2A''$ state, which have the same overall vibronic symmetry. We therefore tentatively assign peak *g* to excitation of the ν_{24} fundamental.

As was true for the $\tilde{X}$ band, the FC envelope for the $\tilde{B}$ state is dominated by the vibrational origin, indicating that photodetachment is accompanied by relatively little change in geometry. The optimized geometries of the anion and $\tilde{B}$ state (Table S1) and the delocalized nature of the Dyson orbital for detachment to the $\tilde{B}$ state (Figure 2c) support this reasoning. While the vibrational features for the $\tilde{X}$ and $\tilde{A}$ states narrow to <15 cm^{-1} fwhm close to threshold, the $\tilde{B}$ state structure is poorly resolved, making assignments intractable beyond identification of the strong vibrational origin. The decaying $\tilde{B}$ state cross section close to threshold allows vibrational features to disappear before they can be narrowly resolved with SEVI.

According to the Wigner threshold law,[58] the near threshold cross section (σ) for photodetachment is a function of both eKE and *l*, the angular momentum of the outgoing photoelectron:

$$\sigma \propto (\mathrm{eKE})^{l+1/2} \qquad (2)$$

Treating the *o*-HPO radical as a pseudo-C_{2v} species with the H_1 atom as a symmetry-breaking perturbation, the $\tilde{B}$ state Dyson orbital has approximate a_2 symmetry. Detachment from an a_2 orbital yields outgoing photoelectrons with angular momentum $l \geq 1$, yielding small σ at small eKE.[59,60] The $\tilde{A}$ state, on the other hand, has a localized *p*-like Dyson orbital, allowing for partial $l = 0$ detachment, and retained σ at low eKE. Calculated photodetachment cross sections of the $\tilde{A}$ and $\tilde{B}$ states (Figure S3) reproduce this difference in threshold behavior.

The poor resolution of vibrational features in the $\tilde{B}$ state is therefore due to a combination of factors, including the low photodetachment cross section at low eKE, dense overlapping $\tilde{A}$ state structure with a nonvanishing threshold cross section, and a significant background of high-eKE photoelectrons from detachment to the radical $\tilde{X}$ state. Additionally, as we invoked HT coupling to assign peak *g* to a FC forbidden vibrational state of $\tilde{A}$, there may be added dense structure above the $\tilde{B}$ vibrational origin from similar vibronic coupling processes, further hampering the resolution and assignment of $\tilde{B}$ state features.

VI. CONCLUSIONS

We have acquired slow photoelectron velocity-map imaging spectra of cold *ortho*-hydroxyphenoxide anions. We observe detailed vibronic structure of the neutral radical, measuring a precise electron affinity of the $\tilde{X}^2A''$ state, and reporting experimental $\tilde{A}^2A'$ and $\tilde{B}^2A''$ excited state term energies for the first time. A number of vibrational frequencies of the radical $\tilde{X}$ and $\tilde{A}$ states are also newly assigned. We demonstrate the efficacy of high-resolution photoelectron imaging in combination with cryogenic ion cooling for untangling the vibronic structure of increasingly complex biorelevant molecules.

■ ASSOCIATED CONTENT

Ⓢ Supporting Information

Full list of calculated geometries and vibrational frequencies for all relevant species, schematics of Franck–Condon active vibrational normal mode displacements, experimental and calculated photoelectron anisotropies for the ground state band, and calculated cross sections for detachment to the excited states of the *ortho*-hydroxyphenoxy radical. This material is available free of charge via the Internet at http://pubs.acs.org.

■ AUTHOR INFORMATION

Corresponding Author

*E-mail: dneumark@berkeley.edu. Phone: 510-642-3635.

Present Address

§SLAC National Accelerator Laboratory, Menlo Park, CA 94025, United States.

Notes

The authors declare no competing financial interest.

■ ACKNOWLEDGMENTS

This work was supported by the Director, Office of Basic Energy Sciences, Chemical Sciences Division of the U.S. Department of Energy under Contract No. DE-AC02-05CH11231. M.L.W. thanks the National Science Foundation for a graduate research fellowship.

■ REFERENCES

(1) Sobolewski, A. L.; Domcke, W.; Dedonder-Lardeux, C.; Jouvet, C. Excited-State Hydrogen Detachment and Hydrogen Transfer Driven by Repulsive $^1\pi\sigma^*$ States: A New Paradigm for Nonradiative Decay in Aromatic Biomolecules. *Phys. Chem. Chem. Phys.* **2002**, *4*, 1093–1100.

(2) Ashfold, M. N. R.; Cronin, B.; Devine, A. L.; Dixon, R. N.; Nix, M. G. D. The Role of $\pi\sigma^*$ Excited States in the Photodissociation of Heteroaromatic Molecules. *Science* **2006**, *312*, 1637–1640.

(3) Ashfold, M. N. R.; King, G. A.; Murdock, D.; Nix, M. G. D.; Oliver, T. A. A.; Sage, A. G. $\pi\sigma^*$ Excited States in Molecular Photochemistry. *Phys. Chem. Chem. Phys.* **2010**, *12*, 1218–1238.

(4) Wright, J. S.; Johnson, E. R.; DiLabio, G. A. Predicting the Activity of Phenolic Antioxidants: Theoretical Method, Analysis of Substituent Effects, and Application to Major Families of Antioxidants. *J. Am. Chem. Soc.* **2001**, *123*, 1173–1183.

(5) Hussain, H. H.; Babic, G.; Durst, T.; Wright, J. S.; Flueraru, M.; Chichirau, A.; Chepelev, L. L. Development of Novel Antioxidants: Design, Synthesis, and Reactivity. *J. Org. Chem.* **2003**, *68*, 7023–7032.

(6) Zhang, H.-Y.; Sung, Y.-M.; Wang, X.-L. Substituent Effects on O–H Bond Dissociation Enthalpies and Ionization Potentials of Catechols: A DFT Study and Its Implications in the Rational Design of Phenolic Antioxidants and Elucidation of Structure-Activity Relationships for Flavonoid Antioxidants. *Chem.—Eur. J.* **2003**, *9*, 502–508.

(7) Leopoldini, M.; Marino, T.; Russo, N.; Toscano, M. Antioxidant Properties of Phenolic Compounds: H-Atom versus Electron Transfer Mechanism. *J. Phys. Chem. A* **2004**, *108*, 4916–4922.

(8) Meredith, P.; Powell, B. J.; Riesz, J.; Nighswander-Rempel, S. P.; Pederson, M. R.; Moore, E. G. Towards Structure-Property-Function Relationships for Eumelanin. *Soft Matter* **2006**, *2*, 37–44.

(9) Meredith, P.; Sarna, T. The Physical and Chemical Properties of Eumelanin. *Pigment Cell Res.* **2006**, *19*, 572–594.

(10) Huijser, A.; Pezzella, A.; Sundström, V. Functionality of Epidermal Melanin Pigments: Current Knowledge on UV-Dissipative Mechanisms and Research Perspectives. *Phys. Chem. Chem. Phys.* **2011**, *13*, 9119–9127.

(11) Pierpont, C. G.; Lange, C. W., The Chemistry of Transition Metal Complexes Containing Catechol and Semiquinone Ligands. In

Prog. Inorg. Chem.; Karlin, K. D., Ed.; John Wiley & Sons, Inc.: Hoboken, NJ, 1994; Vol. *41*, pp 331−442.

(12) King, G. A.; Oliver, T. A. A.; Dixon, R. N.; Ashfold, M. N. R. Vibrational Energy Redistribution in Catechol During Ultraviolet Photolysis. *Phys. Chem. Chem. Phys.* **2012**, *14*, 3338−3345.

(13) Chatterley, A. S.; Young, J. D.; Townsend, D.; Żurek, J. M.; Paterson, M. J.; Roberts, G. M.; Stavros, V. G. Manipulating Dynamics with Chemical Structure: Probing Vibrationally-Enhanced Tunnelling in Photoexcited Catechol. *Phys. Chem. Chem. Phys.* **2013**, *15*, 6879−6892.

(14) Livingstone, R. A.; Thompson, J. O. F.; Iljina, M.; Donaldson, R. J.; Sussman, B. J.; Paterson, M. J.; Townsend, D. Time-Resolved Photoelectron Imaging of Excited State Relaxation Dynamics in Phenol, Catechol, Resorcinol, and Hydroquinone. *J. Chem. Phys.* **2012**, *137*, 18304.

(15) Weiler, M.; Miyazaki, M.; Féraud, G.; Ishiuchi, S.; Dedonder, C.; Jouvet, C.; Fujii, M. Unusual Behavior in the First Excited State Lifetime of Catechol. *J. Phys. Chem. Lett.* **2013**, *4*, 3819−3823.

(16) Loth, K.; Andrist, M.; Graf, F.; Günthard, H. H. Modulated Excitation ESR Spectra of Hydroxy-Phenoxy Radicals. *Chem. Phys. Lett.* **1974**, *29*, 163−168.

(17) Loth, K.; Graf, F.; Günthard, H. H. Chemical Exchange Dynamics and Structure of Intramolecular O−H−O Bridges: An ESR and INDO Study of 2-Hydroxy- and 2,6-Dihydroxy-Phenoxyl. *Chem. Phys.* **1976**, *13*, 95−113.

(18) Nagaya, M.; Kudoh, S.; Nakata, M. Infrared Spectrum of 2-Hydroxyphenoxyl Radical and Photoisomerization Between *Trans* and *Cis* 2-Hydroxyphenyl Nitrites. *Chem. Phys. Lett.* **2006**, *432*, 446−451.

(19) Mebel, A. M.; Lin, M. C. *Ab Initio* Molecular Orbital Calculations of $C_6H_5O_2$ Isomers. *J. Am. Chem. Soc.* **1994**, *116*, 9577−9584.

(20) Lin, M. C.; Mebel, A. M. *Ab Initio* Molecular Orbital Study of the O+C_6H_5O Reaction. *J. Phys. Org. Chem.* **1995**, *8*, 407−420.

(21) Vedernikova, I.; Proynov, E.; Salahub, D.; Haemers, A. Local Atomic and Orbital Reactivity Indices from Density Functional Calculations for Hydrogen-Bonded 1,2-Dihydroxybenzene. *Int. J. Quantum Chem.* **2000**, *77*, 161−173.

(22) Estácio, S. G.; do Couto, P. C.; Cabral, B. J. C.; da Piedade, M. E. M.; Simões, J. A. M. Energetics of Intramolecular Hydrogen Bonding in Di-Substituted Benzenes by the ortho−para Method. *J. Phys. Chem. A* **2004**, *108*, 10834−10843.

(23) McFerrin, C. A.; Hall, R. W.; Dellinger, B. *Ab Initio* Study of the Formation and Degradation Reactions of Semiquinone and Phenoxyl Radicals. *J. Mol. Struct. (THEOCHEM)* **2008**, *848*, 16−23.

(24) Altarawneh, M.; Dlugogorski, B. Z.; Kennedy, E. M.; Mackie, J. C. Thermochemical Properties and Decomposition Pathways of Three Isomeric Semiquinone Radicals. *J. Phys. Chem. A* **2010**, *114*, 1098−1108.

(25) Wang, X.-B.; Fu, Q.; Yang, J. Electron Affinities and Electronic Structures of *o*-, *m*-, and *p*-Hydroxyphenoxyl Radicals: A Combined Low-Temperature Photoelectron Spectroscopic and *Ab Initio* Calculation Study. *J. Phys. Chem. A* **2010**, *114*, 9083−9089.

(26) Parra, R. D.; Dukarevich, I. A Comparative *Ab Initio* Study of Intramolecular Proton Transfer in Model α-Hydroxyalkoxides. *J. Chem. Phys.* **2005**, *122*, 124316.

(27) Binkley, R. W.; Dillow, G. W.; Flechtner, T. W.; Winnik, W.; Tevesz, M. J. S. Fragmentation of Collisionally Activated Hydroxyphenoxide Anions in the Gas Phase. *Org. Mass. Spectrom.* **1994**, *29*, 491−495.

(28) Taylor, W. S.; Babcock, L. M. Gas-Phase Reactions of Catecholate and Related Anions with BF_3 and SiF_4. *J. Am. Chem. Soc.* **1995**, *117*, 6497−6503.

(29) Fattahi, A.; Kass, S. R.; Liebman, J. F.; Matos, M. A. R.; Miranda, M. S.; Morais, V. M. F. The Enthalpies of Formation of *o*-, *m*-, and *p*-Benzoquinone: Gas-Phase Ion Energetics, Combustion Calorimetry, and Quantum Chemical Computations Combined. *J. Am. Chem. Soc.* **2005**, *127*, 6116−6122.

(30) Rienstra-Kiracofe, J. C.; Tschumper, G. S.; Schaefer, H. F.; Nandi, S.; Ellison, G. B. Atomic and Molecular Electron Affinities: Photoelectron Experiments and Theoretical Computations. *Chem. Rev.* **2002**, *102*, 231−282.

(31) Kim, J. B.; Weichman, M. L.; Yacovitch, T. I.; Shih, C.; Neumark, D. M. Slow Photoelectron Velocity-Map Imaging Spectroscopy of the C_9H_7 (Indenyl) and $C_{13}H_9$ (Fluorenyl) Anions. *J. Chem. Phys.* **2013**, *139*, 104301.

(32) Weichman, M. L.; Kim, J. B.; DeVine, J. A.; Levine, D. S.; Neumark, D. M. Vibrational and Electronic Structure of the α- and β-Naphthyl Radicals via Slow Photoelectron Velocity-Map Imaging. *J. Am. Chem. Soc.* **2015**, *137*, 1420−1423.

(33) Kim, J. B.; Yacovitch, T. I.; Hock, C.; Neumark, D. M. Slow Photoelectron Velocity-Map Imaging Spectroscopy of the Phenoxide and Thiophenoxide Anions. *Phys. Chem. Chem. Phys.* **2011**, *13*, 17378−17383.

(34) Osterwalder, A.; Nee, M. J.; Zhou, J.; Neumark, D. M. High Resolution Photodetachment Spectroscopy of Negative Ions via Slow Photoelectron Imaging. *J. Chem. Phys.* **2004**, *121*, 6317−6322.

(35) Neumark, D. M. Slow Electron Velocity-Map Imaging of Negative Ions: Applications to Spectroscopy and Dynamics. *J. Phys. Chem. A* **2008**, *112*, 13287−13301.

(36) Hock, C.; Kim, J. B.; Weichman, M. L.; Yacovitch, T. I.; Neumark, D. M. Slow Photoelectron Velocity-Map Imaging Spectroscopy of Cold Negative Ions. *J. Chem. Phys.* **2012**, *137*, 244201.

(37) Even, U.; Jortner, J.; Noy, D.; Lavie, N.; Cossart-Magos, C. Cooling of Large Molecules Below 1 K and He Clusters Formation. *J. Chem. Phys.* **2000**, *112*, 8068−8071.

(38) Wiley, W. C.; McLaren, I. H. Time-of-Flight Mass Spectrometer with Improved Resolution. *Rev. Sci. Instrum.* **1955**, *26*, 1150−1157.

(39) Eppink, A. T. J. B.; Parker, D. H. Velocity Map Imaging of Ions and Electrons Using Electrostatic Lenses: Application in Photoelectron and Photofragment Ion Imaging of Molecular Oxygen. *Rev. Sci. Instrum.* **1997**, *68*, 3477−3484.

(40) Chandler, D. W.; Houston, P. L. Two-Dimensional Imaging of State-Selected Photodissociation Products Detected by Multiphoton Ionization. *J. Chem. Phys.* **1987**, *87*, 1445−1447.

(41) Doyle, M. B.; Abeyasera, C.; Suits, A. G. *NuACQ*. http://chem.wayne.edu/suitsgroup/NuAcq.html. Accessed January 10, 2015.

(42) Dick, B. Inverting Ion Images without Abel Inversion: Maximum Entropy Reconstruction of Velocity Maps. *Phys. Chem. Chem. Phys.* **2014**, *16*, 570−580.

(43) Blondel, C.; Chaibi, W.; Delsart, C.; Drag, C. The Fine Structure of S and S^- Measured with the Photodetachment Microscope. *J. Phys. B: At. Mol. Opt. Phys.* **2006**, *39*, 1409−1416.

(44) Garand, E.; Neumark, D. M. Study of RgS^- and RgS (Rg = Ne, Ar, and Kr) via Slow Photoelectron Velocity-Map Imaging Spectroscopy and *Ab Initio* Calculations. *J. Chem. Phys.* **2011**, *135*, 024302.

(45) Berzinsh, U.; Gustafsson, M.; Hanstorp, D.; Klinkmüller, A.; Ljungblad, U.; Mårtensson-Pendrill, A.-M. Isotope Shift in the Electron Affinity of Chlorine. *Phys. Rev. A* **1995**, *51*, 231−238.

(46) Gilbert, A. T. B.; Besley, N. A.; Gill, P. M. W. Self-Consistent Field Calculations of Excited States Using the Maximum Overlap Method (MOM). *J. Phys. Chem. A* **2008**, *112*, 13164−13171.

(47) Shao, Y.; Molnar, L. F.; Jung, Y.; Kussmann, J.; Ochsenfeld, C.; Brown, S. T.; Gilbert, A. T. B.; Slipchenko, L. V.; Levchenko, S. V.; O'Neill, D. P.; et al. Advances in Methods and Algorithms in a Modern Quantum Chemistry Program Package. *Phys. Chem. Chem. Phys.* **2006**, *8*, 3172−3191.

(48) Krylov, A. I.; Gill, P. M. W. Q-Chem: An Engine for Innovation. *WIREs Comput. Mol. Sci.* **2013**, *3*, 317−326.

(49) Gunion, R. F.; Gilles, M. K.; Polak, M. L.; Lineberger, W. C. Ultraviolet Photoelectron Spectroscopy of the Phenide, Benzyl and Phenoxide Anions, with *Ab Initio* Calculations. *Int. J. Mass Spectrom. Ion Processes* **1992**, *117*, 601−620.

(50) Cheng, C. W.; Witek, H.; Lee, Y. P. Rovibronic Bands of the $\tilde{A}\,{}^2B_2 \leftarrow \tilde{X}\,{}^2B_1$ Transition of C_6H_5O and C_6D_5O Detected with Cavity Ringdown Absorption Near 1.2 μm. *J. Chem. Phys.* **2008**, *129*, 154307.

(51) Runge, E.; Gross, E. K. U. Density-Functional Theory for Time-Dependent Systems. *Phys. Rev. Lett.* **1984**, *52*, 997−1000.

(52) Mozhayskiy, V. A.; Krylov, A. I. *ezSpectrum 3.0*. http://iopenshell.usc.edu/downloads. Accessed January 10, 2015.

(53) Duschinsky, F. On the Interpretation of Electronic Spectra of Polyatomic Molecules. I. Concerning the Franck-Condon Principle. *Acta Physicochim. URSS* **1937**, *7*, 551−566.

(54) Tao, L.; Oana, C. M.; Mozhayskiy, V. A.; Krylov, A. I. *ezDyson 2.0*. http://iopenshell.usc.edu/downloads/ezdyson. Accessed January 10, 2015.

(55) Oana, C. M.; Krylov, A. I. Cross Sections and Photoelectron Angular Distributions in Photodetachment from Negative Ions using Equation-of-Motion Coupled-Cluster Dyson Orbitals. *J. Chem. Phys.* **2009**, *131*, 124114.

(56) Weichman, M. L.; Kim, J. B.; Neumark, D. M. Vibrational Fine Structure of C_5 via Anion Slow Photoelectron Velocity-Map Imaging. *J. Chem. Phys.* **2013**, *139*, 144314.

(57) Cooper, J.; Zare, R. N. Angular Distribution of Photoelectrons. *J. Chem. Phys.* **1968**, *48*, 942−943.

(58) Wigner, E. P. On the Behavior of Cross Sections Near Thresholds. *Phys. Rev.* **1948**, *73*, 1002−1009.

(59) Mabbs, R.; Grumbling, E. R.; Pichugin, K.; Sanov, A. Photoelectron Imaging: An Experimental Window into Electronic Structure. *Chem. Soc. Rev.* **2009**, *38*, 2169−2177.

(60) Reed, K. J.; Zimmerman, A. H.; Andersen, H. C.; Brauman, J. I. Cross Sections for Photodetachment of Electrons from Negative Ions near Threshold. *J. Chem. Phys.* **1976**, *64*, 1368−1375.